

An Excited Dark Matter Solution to the MeV Galactic Center Excesses

SHYAM BALAJI,¹ DAMON CLEAVER,¹ AND PEDRO DE LA TORRE LUQUE^{2,3}

¹*Physics Department, King's College London, Strand, London, WC2R 2LS, United Kingdom*

²*Departamento de Física Teórica, M-15, Universidad Autónoma de Madrid, E-28049 Madrid, Spain*

³*Instituto de Física Teórica UAM-CSIC, Universidad Autónoma de Madrid, C/ Nicolás Cabrera, 13-15, 28049 Madrid, Spain*

ABSTRACT

Recent COMPTEL data analysis reveals a ~ 2 MeV continuum excess whose spatial distribution closely matches the long-standing 511 keV line observed by INTEGRAL/SPI, indicating a common population of low-energy positrons that is difficult to reconcile with known astrophysical sources or standard thermal dark matter (DM). We show that a minimal Excited Dark Matter (XDM) model naturally explains these features. In this scenario a DM particle χ is inelastically upscattered into an excited state χ^* , followed by de-excitation $\chi^* \rightarrow \chi e^+ e^-$ producing ~ 2 MeV positrons that reproduce the 511 keV line morphology and the COMPTEL MeV continuum. Using a full cosmic-ray (CR) propagation treatment, we obtain an excellent fit for $m_\chi \simeq 1.5$ TeV DM particle with mass-splitting $\Delta m = m_{\chi^*} - m_\chi \simeq 4$ MeV for an inelastic geometric scattering cross section of $\sigma_{\text{mr}} = 3\text{--}4 \times 10^{-23} \text{ cm}^2$. The same positrons supply a substantial, radially flat contribution to the anomalous Central Molecular Zone (CMZ) ionization rate. This is the first unified treatment of XDM-induced positrons across all three observables, yielding correlated MeV signatures testable by upcoming missions targeting the Galactic MeV band.

1. INTRODUCTION

The Galactic 511 keV annihilation line has remained one of the most persistent puzzles in high-energy astrophysics for decades. INTEGRAL/SPI measurements (Prantzos *et al.* 2011; Kierans *et al.* 2019; Siegert *et al.* 2019; Siegert 2023) reveal a bright, nearly symmetric emission around the Galactic Center (GC) and extending $\sim 6^\circ\text{--}8^\circ$ on the sky. The inferred positron injection rate, $R_{e^+} \sim 10^{43} \text{ s}^{-1}$ (Prantzos *et al.* 2011), together with the narrow extension of the signal, implies injection energies below a few–tens of MeV.

shyam.balaji@kcl.ac.uk

damon.cleaver@kcl.ac.uk

pedro.delatorre@uam.es

While β^+ decays of ^{26}Al , ^{44}Ti and ^{56}Ni can account for a substantial fraction of the disk component (Diehl *et al.* 2006; Prantzos *et al.* 2011), conventional astrophysical populations struggle to reproduce the bright, compact bulge emission (Siegert 2023). Stellar templates such as the nuclear stellar bulge or a boxy bulge can be tuned to match the observed morphology (Siegert *et al.* 2021), which has been interpreted as support for a stellar origin. However, magnetohydrodynamic simulations of Milky Way–like galaxies show that dark matter (DM)–baryon interactions can drive the DM distribution into a configuration that closely traces the stellar bulge and boxy bulge structure (Muru *et al.* 2025). In such cases, template fits based solely on stellar tracers cannot reliably distinguish a purely stellar explanation from one in which DM contributes significantly.

The DM interpretation of the 511 keV line has therefore received sustained attention (Boehm *et al.* 2004; Vincent

et al. 2012; De la Torre Luque *et al.* 2025, 2024; De la Torre Luque; Pedro *et al.* 2025; Nguyen *et al.* 2025). Simple *s*-wave annihilation scenarios, in which MeV-scale DM directly produces e^+e^- pairs, are tightly constrained by CMB and Big Bang Nucleosynthesis (Beacom and Yuksel 2006; Sizun *et al.* 2007; Wilkinson *et al.* 2016; De la Torre Luque *et al.* 2025), disfavoring standard thermal MeV DM as the source of the positrons (however, see Ref. (Aghaie *et al.* 2025) for an interesting possibility which evades current constraints and is able to reproduce the 511 keV observations).

A particularly promising alternative is the *Excited Dark Matter* (XDM) framework proposed in Finkbeiner and Weiner (2007). In this scenario, collisions between DM particles inelastically excite one particle to a slightly heavier state that decays back via a light mediator, producing an e^+e^- pair. Because excitation requires a threshold in relative velocity, the positron production rate acquires an exponential dependence on the local velocity dispersion. As the halo velocity dispersion decreases with galactocentric radius, the upscattering rate is strongly suppressed outside the inner kiloparsec, yielding a bulge-peaked morphology that naturally declines toward the disk. Quantitative studies by Vincent *et al.* (2012) and Cappiello *et al.* (2023) showed that such XDM models can reproduce the INTEGRAL/SPI angular profile for TeV-scale DM masses, providing a markedly better fit than standard annihilating DM scenarios.

In parallel, a reanalysis of archival COMPTEL data has uncovered a broad excess around 2–3 MeV, detected at $\sim 8\sigma$ significance and consistent with in-flight annihilation (IfA) of ~ 2 MeV positrons (Knöldseder *et al.* 2025). The spatial distribution of this MeV excess closely tracks the 511 keV emission, strongly suggesting a common source of low-energy positrons.

A third anomaly arises in the Central Molecular Zone (CMZ), the dense neutral-gas complex within the central few hundred parsecs of the Galaxy. Multiple molecular tracers indicate an H_2 ionization rate $\zeta_{\text{H}_2} \gtrsim 10^{-15} \text{ s}^{-1}$ (Oka *et al.* 2005; Oka and Geballe 2020), which is difficult to reconcile with standard CRs (cosmic rays): they are strongly attenuated in dense clouds and their predicted ionization rate falls short by at least two orders of magnitude (Ravikularaman *et al.* 2025; Huang *et al.* 2021). Moreover, ionization powered by a single central source such as Sgr A* or HESS J1745-290 is expected to peak sharply near the source and decline steeply with radius, whereas the data favour a much flatter radial profile across the CMZ (Dogiel *et al.* 2013; Ravikularaman *et al.* 2025). De la Torre Luque *et al.* (2025) showed that MeV DM annihilating into e^\pm can efficiently ionize the CMZ and reproduce both the level and approximate flatness of the ionization profile, in a region of parameter space compatible with existing constraints and with

positron injection rates comparable to those required for the 511 keV line.

In this work we show that a minimal XDM model can simultaneously account for all three Galactic observables: the INTEGRAL/SPI 511 keV morphology, the COMPTEL 2–3 MeV IfA excess, and a substantial fraction of the anomalous CMZ ionization rate. We focus on TeV-scale m_χ and few-MeV mass splittings Δm , where threshold-suppressed inelastic upscattering reproduces the observed bulge-dominated morphology and the associated ~ 2 MeV positron population naturally yields both the IfA continuum and an approximately radially flat ionization profile in the CMZ.

We perform, the first full CR propagation analysis of the XDM scenario, implementing the injected e^\pm spectrum in the DRAGON2 framework to model transport, cooling and annihilation in the Galactic environment. This framework refines the 511 keV morphology which we then apply to the higher-energy IfA component, providing the first XDM-based explanation of the ~ 2 –3 MeV COMPTEL bump. We then finally compute the contribution of these electrons and positrons to the CMZ ionization rate.

The remainder of this paper is organised as follows. Section 2 summarizes the XDM mechanism, introduces the key phenomenological parameters and describes our implementation of the excitation rate and positron source term. Section 3 presents the fit to the 511 keV line, and the prediction of the IfA signal and the CMZ ionization contribution. Section 4 discusses the implications of our results and the prospects for testing this scenario with future MeV-band observations.

2. EXCITED DARK MATTER FRAMEWORK

Overview and Physical Picture

We consider a minimal dark sector with two nearly degenerate states: a stable ground state χ and a slightly heavier excited state χ^* , separated by a small mass splitting $\Delta m = m_{\chi^*} - m_\chi$. This setup, first proposed for the 511 keV line in Finkbeiner and Weiner (2007) and revisited in Vincent *et al.* (2012); Cappiello *et al.* (2023), provides a simple way for DM to produce low-energy positrons in the Milky Way.

Collisions between DM particles can inelastically upscatter one of them to the excited state, $\chi\chi \rightarrow \chi\chi^*$ provided their relative velocity exceeds a kinematic threshold. The excited state then decays $\chi^* \rightarrow \chi e^+e^-$, releasing an e^+e^- pair with total energy $\sim \Delta m$. In contrast to standard annihilating DM, this mechanism converts a small fraction of the halo *kinetic* energy into electron–positron pairs, leaving the overall DM abundance and large-scale halo structure unchanged. Even if only a tiny fraction of

particles are excited per Hubble time, the kinetic energy reservoir is sufficient to power the observed positron production rate in the Galactic bulge (Prantzos *et al.* 2011; Siegert 2023).

Each upscattering event injects positrons with kinetic energy $E_{e+} \simeq \Delta m/2$, so $\Delta m \sim \text{few MeV}$ naturally yields non-relativistic positrons consistent with the narrow 511 keV line. The strong velocity threshold induces a steep radial dependence in the excitation rate: because the velocity dispersion $\sigma_v(r)$ decreases with galactocentric radius, the upscattering rate is exponentially suppressed beyond the inner kiloparsec. This produces a sharply peaked, bulge-dominated morphology that matches the $\sim 6 - 8^\circ$ FWHM of the INTEGRAL/SPI signal (Weidenspointner *et al.* 2007; Siegert *et al.* 2019) without requiring ad hoc modifications of the DM density profile.

The excitation process is kinematically inaccessible in the early Universe and does not affect the relic abundance. Freeze-out proceeds through standard annihilation channels, such as $\chi\chi \rightarrow \phi\phi$ or $\chi\chi \rightarrow \text{SM}$, with $\langle\sigma v\rangle_{\text{fo}} \simeq 3 \times 10^{-26} \text{ cm}^3 \text{s}^{-1}$, giving the observed DM density. The late-time inelastic channel is then enhanced at halo velocities (for example by Sommerfeld enhancement in the presence of a light mediator) without violating cosmological constraints. To remain in the perturbative regime, the fitted cross section must satisfy the unitarity bound $\sigma_{\text{mr}} \lesssim 4\pi/m_\phi^2$ where m_ϕ denotes the light mediator mass.

Kinematics and Excitation Threshold

The upscattering process $\chi\chi \rightarrow \chi\chi^*$ is kinematically allowed only if the relative velocity exceeds a threshold

$$v_{\text{th}} = \sqrt{\frac{4\Delta m}{m_\chi}}. \quad (1)$$

For benchmark values $m_\chi \sim 1 \text{ TeV}$ and $\Delta m \sim 4 \text{ MeV}$, one finds $v_{\text{th}} \simeq 1200 \text{ km s}^{-1}$, which is significantly larger than the velocity dispersion in the inner halo. Only a small fraction of particle pairs in the central few hundred parsecs therefore possess sufficient kinetic energy to excite, and the rate falls steeply with radius as $\sigma_v(r)$ decreases.

This velocity selectivity distinguishes XDM from standard annihilation models. While conventional annihilation scales as $\rho_\chi^2(r)$, the positron production rate acquires an additional exponential cutoff from the velocity distribution,

$$R_{e+}(r) \propto \rho_\chi^2(r) \exp\left[-\frac{v_{\text{th}}^2}{4\sigma_v^2(r)}\right], \quad (2)$$

as shown in Finkbeiner and Weiner (2007); Vincent *et al.* (2012); Cappiello *et al.* (2023). The exponential factor arises from integrating the inelastic cross section over the local Maxwell-Boltzmann velocity distribution and naturally suppresses the signal outside the Galactic bulge.

At the microscopic level, we parameterize the inelastic upscattering cross section as (Cappiello *et al.* 2023)

$$\sigma v_{\text{rel}} = \begin{cases} \sigma_{\text{mr}} \sqrt{v_{\text{rel}}^2 - v_{\text{th}}^2}, & v_{\text{rel}} > v_{\text{th}}, \\ 0, & v_{\text{rel}} \leq v_{\text{th}}, \end{cases} \quad (3)$$

where σ_{mr} sets the normalization of the inelastic scattering cross section in the moderately relativistic limit. The threshold v_{th} introduces a sharp kinematic cutoff, confining excitations to the high-velocity tail of the halo distribution and imprinting the exponential suppression with radius seen in Eq. (2). This form approximates the more general expressions obtained in light-mediator models (Finkbeiner and Weiner 2007; Pospelov and Ritz 2007; Arkani-Hamed *et al.* 2009), while capturing the astrophysically relevant dependence needed to model the Galactic signal.

In what follows, we fold this threshold behaviour into a full computation of the velocity-averaged excitation rate using the local velocity dispersion $\sigma_v(r)$ derived from the Jeans equation (Section 2.0). This quantity controls both the radial morphology of the 511 keV emission and the total positron injection rate relevant for the IfA and CMZ analyses.

Positron Injection Rate

The local positron production rate per unit volume from inelastic DM upscattering is

$$Q_{e+}(r, E_e) = \frac{\rho_\chi^2(r)}{2m_\chi^2} \langle\sigma v\rangle(r) \frac{dN}{dE}(E_e), \quad (4)$$

where $\rho_\chi(r)$ is the DM density profile, m_χ is the particle mass, and the spectrum $dN/dE_e = 2\delta(E - \Delta m/2)$ for monoenergetic injection. The factor of 1/2 avoids double-counting identical initial states. This source term drives all of the subsequent phenomenology.

Velocity-averaged excitation rate. Following Cappiello *et al.* (2023), the velocity-averaged inelastic excitation cross section is obtained by integrating the microscopic cross section over the local DM velocity distribution,

$$\langle \sigma v \rangle = \sigma_{\text{mr}} 2\pi \left(\frac{1}{N_{\text{esc}}} \frac{1}{(2\pi\sigma_v^2)^{3/2}} \right)^2 \times \int_{v_{\text{th}}}^{2v_{\text{esc}}} dv_{\text{rel}} v_{\text{rel}} \sqrt{v_{\text{rel}}^2 - v_{\text{th}}^2} e^{-\frac{2v_{\text{esc}}^2 + v_{\text{rel}}^2}{2\sigma_v^2}} \sigma_v^3 \left[2\sigma_v (e^{\frac{v_{\text{rel}}^2}{2\sigma_v^2}} - e^{-\frac{v_{\text{esc}} v_{\text{rel}}}{2\sigma_v^2}}) + \sqrt{\pi} v_{\text{rel}} e^{\frac{4v_{\text{esc}}^2 + v_{\text{rel}}^2}{4\sigma_v^2}} \text{erf} \left(\frac{2v_{\text{esc}} - v_{\text{rel}}}{2\sigma_v} \right) \right], \quad (5)$$

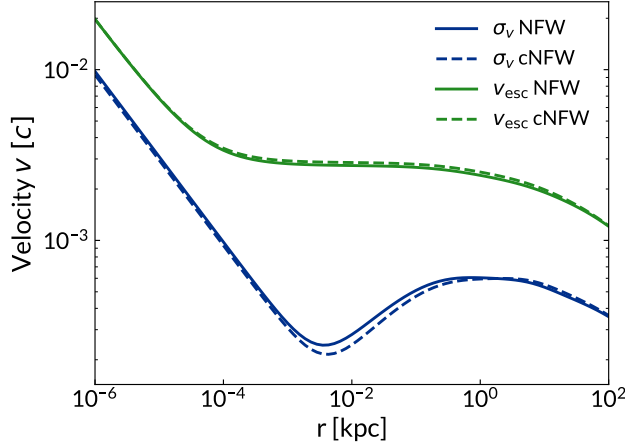


Figure 1. DM velocity profiles as a function of radial distance from the GC for the velocity dispersion σ_v (blue) and escape velocity v_{esc} (green) for NFW (solid) and cNFW (dashed) DM density distributions. The cNFW profile has inner slope $\gamma = 1.2$.

where $\sigma_v(r)$ and $v_{\text{esc}}(r)$ are the local DM velocity dispersion and escape velocity, and N_{esc} normalizes the truncated Maxwellian distribution. The threshold velocity v_{th} is defined in Eq. (1).¹

Velocity Dispersion and Escape Velocity

The velocity dispersion $\sigma_v(r)$ and escape velocity $v_{\text{esc}}(r)$ entering Eq. (5) are shown in Fig. 1. They are computed by solving the isotropic Jeans equation under spherical symmetry, following [Vincent et al. \(2012\)](#); [Cappiello et al. \(2023\)](#). The total gravitational potential includes contributions from DM, bulge, disk and

¹ In Eq. (5) of [Cappiello et al. \(2023\)](#), a cross section $\langle \sigma v \rangle_{\text{mr}} \simeq \sigma_{\text{mr}} v_{\text{eff}}$ was introduced as a constant normalization with an effective halo velocity $v_{\text{eff}} \sim 10^{-3}c$. Here we instead derive $\langle \sigma v \rangle(r)$ by explicitly integrating over the full velocity distribution, which is appropriate for a geometric cross section σ_{mr} and ensures a self-consistent radial dependence.

Sgr A*. We adopt the same baryonic potential models and parameter choices as [Vincent et al. \(2012\)](#), which reproduce Milky Way rotation-curve data and yield $\sigma_v \sim 200\text{--}250 \text{ km s}^{-1}$ and $v_{\text{esc}} \sim 600\text{--}700 \text{ km s}^{-1}$ in the inner kiloparsec.

511 keV Morphology and Positron Propagation

The angular distribution of 511 keV photons is obtained by integrating the local emissivity of diffuse positrons along the line of sight. Unlike previous morphology studies that assumed instantaneous annihilation at the production site ([Vincent et al. 2012](#); [Cappiello et al. 2023](#)), we propagate positrons with non-zero kinetic energy using the DRAGON2 code, following [De la Torre Luque et al. \(2024\)](#). This includes diffusion, reacceleration and energy losses, and yields a steady-state positron distribution before annihilation.

The resulting flux per unit solid angle over line-of-sight distance s for a position (x, y, z) is

$$\frac{d\phi_{\gamma}^{511}}{d\Omega} = 2 k_{\text{ps}} \int ds s^2 \frac{\epsilon_e(x_{s,b,l}, y_{s,b,l}, z_{s,b,l})}{4\pi s^2}, \quad (6)$$

where $k_{\text{ps}} = 1/4$ is the fraction of positronium that decays into para-positronium producing two 511 keV photons. The quantity ϵ_e is the line emissivity,

$$\epsilon_e = \frac{d\phi_e}{dE}(E_{\text{th}}) n_e \sigma^{\text{ps}}(E_{\text{th}}), \quad (7)$$

where $\frac{d\phi_e}{dE}(E_{\text{th}})$ is the propagated positron flux at thermal energy E_{th} , σ^{ps} is the charge-exchange cross section for positronium formation with hydrogen ([Jean, P. et al. 2009](#)), and n_e is the ambient electron density. We take $n_e = 1 \text{ cm}^{-3}$ in the Galactic plane and adopt an exponential decrease above and below the plane as in [De la Torre Luque; Pedro et al. \(2025\)](#), combining a Nakanishi warm-gas component ([Nakanishi and Sofue 2003](#)) and a Ferriere hot-gas component ([Ferriere 1998](#)).

This treatment correctly accounts for the finite propagation length of injected MeV positrons, producing a slightly more extended bulge emission than instantaneous-annihilation models.

In-Flight Annihilation Excess

Relativistic positrons injected in the interstellar medium can annihilate with electrons before becoming thermal, producing a continuum of γ rays up to the positron energy. IfA has long been recognized as a probe of MeV DM scenarios (Stecker 1969; Beacom and Yuksel 2006; Sizun *et al.* 2006), since high injection energies generate an IfA flux that can overshoot the observed diffuse MeV background (Strong *et al.* 1994; Bouchet *et al.* 2011).

As discussed in Sec. 1, the reanalysis of COMPTEL data by Knöldlseder *et al.* (2025) reveals a MeV excess consistent with IfA of ~ 2 MeV positrons sharing the 511 keV spatial template. In our XDM scenario, these positrons are produced in $\chi^* \rightarrow \chi e^+ e^-$ decays with injection energy $E_{e^+} \simeq \Delta m/2$. For monoenergetic injection, the differential IfA γ -ray flux can be related to the 511 keV intensity (Beacom and Yuksel 2006; Beacom *et al.* 2005):

$$\frac{d\Phi^{\text{IfA}}}{dE_\gamma} = \frac{\Phi^{511}}{1 - f_{\text{Ps}}/4} P^{\text{IfA}}(E_\gamma; E_0, n_e), \quad (8)$$

where $f_{\text{Ps}} \simeq 0.97$ is the positronium fraction (Jean, P. *et al.* 2009; Bouchet *et al.* 2010) and $P^{\text{IfA}}(E_\gamma; E_0, n_e)$ is the photon spectrum per injected positron of initial energy $E_0 = \Delta m/2$ in a medium of density n_e .

Here we compute the IfA signal following De la Torre Luque; Pedro *et al.* (2025), using the steady-state positron spectrum obtained from DRAGON2:

$$\begin{aligned} \frac{d\Phi^{\text{IfA}}}{d\Omega dE_\gamma} &= \frac{d\Phi^{511}}{d\Omega} \frac{n_H}{P(1 - \frac{3}{4}f_{\text{Ps}})} \\ &\times \int_{E_\gamma=m_e/2}^{E_{\text{max}}} dE' \frac{1}{N_{\text{pos}}} \frac{dN_{\text{pos}}}{dE'} \\ &\times \int_{m_e}^{E'} P_{E' \rightarrow E} \frac{d\sigma}{dE_\gamma} \frac{dE}{|dE/dx|}, \end{aligned} \quad (9)$$

where the first integral over E' accounts for the propagated positron energy distribution, bounded between E_{max} (the maximum steady-state energy) and $m_e/2$ (Bartels *et al.* 2017). The factor $(1/N_{\text{pos}}) dN_{\text{pos}}/dE'$ gives the fraction of positrons at energy E' that contribute to the 511 keV emission. The hydrogen density n_H sets the number of target electrons, $P_{E' \rightarrow E}$ is the probability for a positron to produce a photon before cooling from E' to E (Beacom and Yuksel 2006), and $P = P_{E' \rightarrow m_e}$ is the total probability to emit a photon before reaching thermal energies.

Ionization of the Central Molecular Zone

As discussed in Sec. 1, multiple molecular tracers indicate an H_2 ionization rate in the CMZ of $\zeta_{\text{H}_2} \gtrsim 10^{-15} \text{ s}^{-1}$ with an approximately flat radial profile (Oka *et al.* 2005; Oka and Geballe 2020; Dogiel *et al.* 2013; Ravikularaman

et al. 2025), which is difficult to explain with standard CRs alone (Huang *et al.* 2021; Ravikularaman *et al.* 2025). In light of the MeV-DM explanation proposed by De la Torre Luque *et al.* (2025), we now ask whether the same XDM setup that fits the 511 keV morphology and IfA signal can also contribute appreciably to the CMZ ionisation.

We follow De la Torre Luque *et al.* (2025) to compute the H_2 ionization rate ζ_{H_2} caused by the e^\pm pairs emitted in XDM de-excitations inside the CMZ. The rate is

$$\zeta_{\text{H}_2} = 2 \cdot 4\pi \int_{E_{\text{min}}}^{E_{\text{max}}} J(E, \mathbf{x}) \sigma(E) (1 + \theta_e(E)) dE, \quad (10)$$

where the prefactor 2 accounts for ionization by both e^- and e^+ , $E_{\text{max}} = \Delta m/2$ is the injection energy, and E_{min} is the threshold for ionization in H_2 (15.43 eV (Padovani *et al.* 2009)). The cross section $\sigma(E)$ is the electron- H_2 ionization cross section, calculated as in Eq. (7) of Padovani *et al.* (2009), and $\theta_e(E)$ is the number of secondary ionizations per primary ionization, from Eq. (2.23) of Krause *et al.* (2015). The flux $J(E, \mathbf{x})$ is the propagated e^\pm flux from DRAGON2, which includes the strong energy losses suffered by these particles in the CMZ. Typical propagation distances before thermalization are of order tens of parsecs, depending on the injection energy.

This formalism allows us to compute the radial profile of the XDM-induced ionization rate across the CMZ and to quantify its contribution relative to the observed anomaly.

3. RESULTS

Fit to the 511 keV Morphology

We compare the 511 keV flux from Eq. (6) with INTEGRAL/SPI data, which provide fluxes binned in Galactic longitude l and latitude b . Following Siegert (2023), we construct a longitude profile by binning in 3° intervals in l and integrating over $-10.75^\circ < b < 10.25^\circ$, and a latitude profile by binning in 3° intervals in b and integrating over $-5.25^\circ < l < 3.75^\circ$. For a given XDM model, we define

$$\begin{aligned} \chi^2 &= \sum_b \frac{[\phi_{\gamma,b}^{511}(\sigma_{\text{mr}}) - \phi_{\text{SPI},b}]^2}{\sigma_{\text{SPI},b}^2} \\ &+ \sum_l \frac{[\phi_{\gamma,l}^{511}(\sigma_{\text{mr}}) - \phi_{\text{SPI},l}]^2}{\sigma_{\text{SPI},l}^2}, \end{aligned} \quad (11)$$

where $\phi_{\gamma,i}^{511}(\sigma_{\text{mr}})$ is the predicted XDM flux in bin i , and $\phi_{\text{SPI},i}$ and $\sigma_{\text{SPI},i}$ are the measured flux and uncertainty. Varying σ_{mr} we obtain the best-fit value for each choice of $(m_\chi, \Delta m)$, which is then used to compute the IfA spectrum and CMZ ionization.

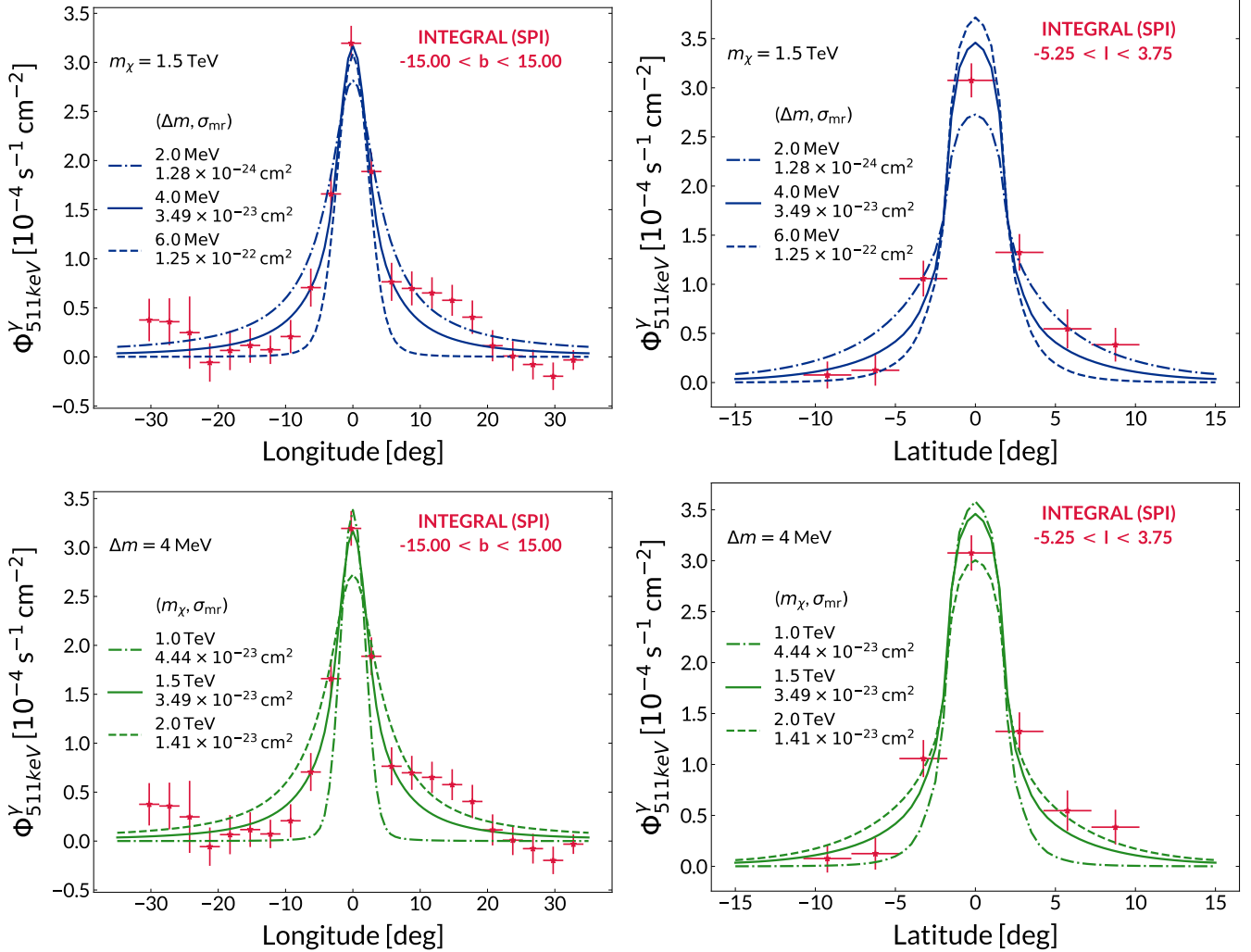


Figure 2. 511 keV longitude profiles (left panels) and latitude profiles (right panels) for XDM models compared to INTEGRAL/SPI data (red points). Top: fixed $m_\chi = 1.5$ TeV and varying mass splittings Δm . Bottom: fixed $\Delta m = 4$ MeV and varying m_χ .

The top panels of Fig. 2 show the effect of varying the mass splitting between 2 and 6 MeV for fixed $m_\chi = 1.5$ TeV. All of these splittings can, in principle, produce an IfA signal compatible with COMPTEL, but they imprint distinct 511 keV morphologies. The dominant effect is the change in the threshold velocity v_{th} , which controls the radial range over which upscattering is efficient. A secondary effect arises from the different positron injection energies, which slightly modify the diffusion length, since the diffusion coefficient is energy dependent.

The bottom panels of Fig. 2 show the longitude and latitude profiles for fixed $\Delta m = 4$ MeV and varying m_χ . This choice of splitting produces monoenergetic positrons with $E_{e^\pm} = \Delta m/2 = 2$ MeV, which is the best-fit injection energy for the bulge component of the IfA spectrum in Knölseder *et al.* (2025). For $m_\chi = 1.5$ TeV and $\Delta m = 4$ MeV we obtain an excellent fit to the

SPI morphology with a reduced chi-squared of $\chi_{\text{red}}^2 \simeq 1.5$ for an NFW profile, even without invoking the IfA or CMZ constraints.

For fixed Δm and an NFW density profile, increasing m_χ broadens the emission. Eq. (1) shows that higher masses lowers the inelastic threshold, so upscattering remains kinematically allowed out to larger radii where the velocity dispersion is smaller. This enhances the velocity-averaged excitation rate coefficient $\langle \sigma v \rangle(r)$ at larger r , and smooths the longitude and latitude profiles. Lower masses, by contrast, produce cuspier 511 keV profiles more strongly concentrated toward the GC.

At low m_χ the predicted bulge emission peaks sharply around the GC and can still be made compatible with SPI data once a disk component from astrophysical positron sources is included, such as massive stars or SNe, following Cappiello *et al.* (2023); De la Torre Luque; Pedro

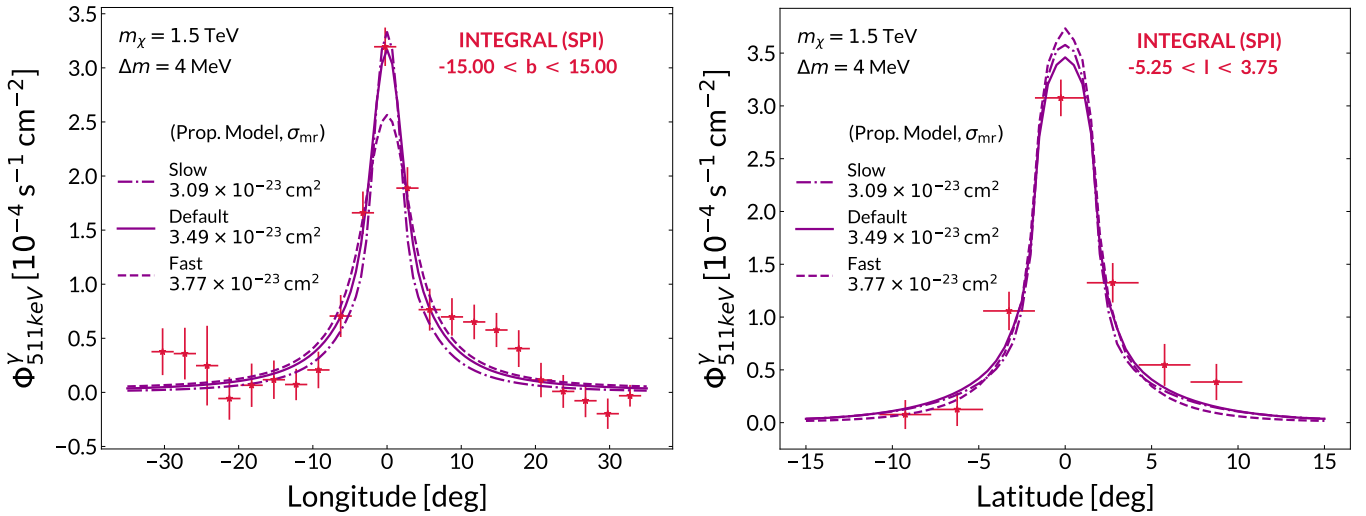


Figure 3. 511 keV longitude (left) and latitude (right) profiles for XDM with $m_\chi = 1.5$ TeV and $\Delta m = 4$ MeV, compared to INTEGRAL/SPI data (red points), for three propagation setups: “Default” (solid), “Fast” (dashed) and “Slow” (dash-dotted), following De la Torre Luque *et al.* (2024).

et al. (2025). Such a disk component is guaranteed at some level, although its modelling carries significant uncertainties. Conversely, a cuspier DM profile naturally yields a cuspier 511 keV morphology and allows larger m_χ to remain compatible with SPI. This is illustrated in Fig. 6, where we compare the NFW case to a contracted NFW (cNFW) profile with inner slope $\gamma = 1.2$. In this case the density profile, the velocity dispersion and escape velocity (Fig. 1), and thus the radial dependence of $\langle \sigma v \rangle$ from Eq. (5), are all modified.

Propagation Uncertainties

Fig. 3 shows the impact of CR propagation uncertainties on the 511 keV morphology. We consider the “Fast”, “Default” and “Slow” models of De la Torre Luque *et al.* (2024), which bracket optimistic and pessimistic choices for the diffusion and energy-loss parameters. The resulting differences in the longitude and latitude profiles are modest, reflecting the low kinetic energy of the injected positrons: their transport is dominated by energy losses rather than spatial diffusion. The main conclusions regarding the XDM fit to SPI are therefore robust against reasonable variations of the propagation setup.

In-Flight Annihilation Spectrum

Using the best-fit cross sections σ_{mr} obtained from the 511 keV morphology for the models in Fig. 2, we compute the corresponding IfA spectra in the COMPTEL energy range. The top panels of Fig. 4 compare the all-sky XDM-induced emission to the bulge excess extracted by Knöldlseder *et al.* (2025). Internal bremsstrahlung (IB) associated with the outgoing e^\pm is included following Eq. (2) of Beacom *et al.* (2005), with m_χ replaced by

$\Delta m/2$, the positron energy. The separate IB and IfA components for our fiducial model are shown in the bottom panel.

For our default benchmark $m_\chi = 1.5$ TeV and $\Delta m = 4$ MeV, the predicted XDM signal is remarkably consistent with the COMPTEL data within 1σ across the MeV bump. The integrated 511 keV photon flux in this case is

$$\Phi_{511} \simeq 1.1 \times 10^{-4} \text{ ph s}^{-1} \text{ cm}^{-2}, \quad (12)$$

while the best-fit value reported by Knöldlseder *et al.* (2025) for a conventional 2.1 MeV annihilating DM scenario (including IB) is $\Phi_{511} = 1.4 \times 10^{-4} \text{ ph s}^{-1} \text{ cm}^{-2}$. Given the systematic uncertainties inherent to the 511 keV measurement and the modelling of the IfA signal, this level of agreement indicates that the XDM framework passes a non-trivial consistency check: the values of σ_{mr} required to fit the SPI morphology also predict an MeV continuum compatible with the COMPTEL excess.

The left panel of Fig. 7 shows the IfA spectrum for the cNFW profile, for $m_\chi = 1.5$ and 2 TeV. In this case the total IfA flux is lower than in the NFW case because the more concentrated DM profile forces the 511 keV fit to be obtained with a smaller cross section σ_{mr} in order not to overshoot the SPI flux in the inner region. This directly translates into a reduced IfA emission.

Ionization of the Central Molecular Zone

Fig. 5 shows the ionization rate $\zeta(R)$ in the CMZ obtained from Eq. (10) using the propagated XDM-induced e^\pm fluxes from DRAGON2. For a fixed splitting $\Delta m = 4$ MeV and an NFW profile, the predicted ionization rates reach a few $\times 10^{-16} \text{ s}^{-1}$ inside the CMZ, above standard

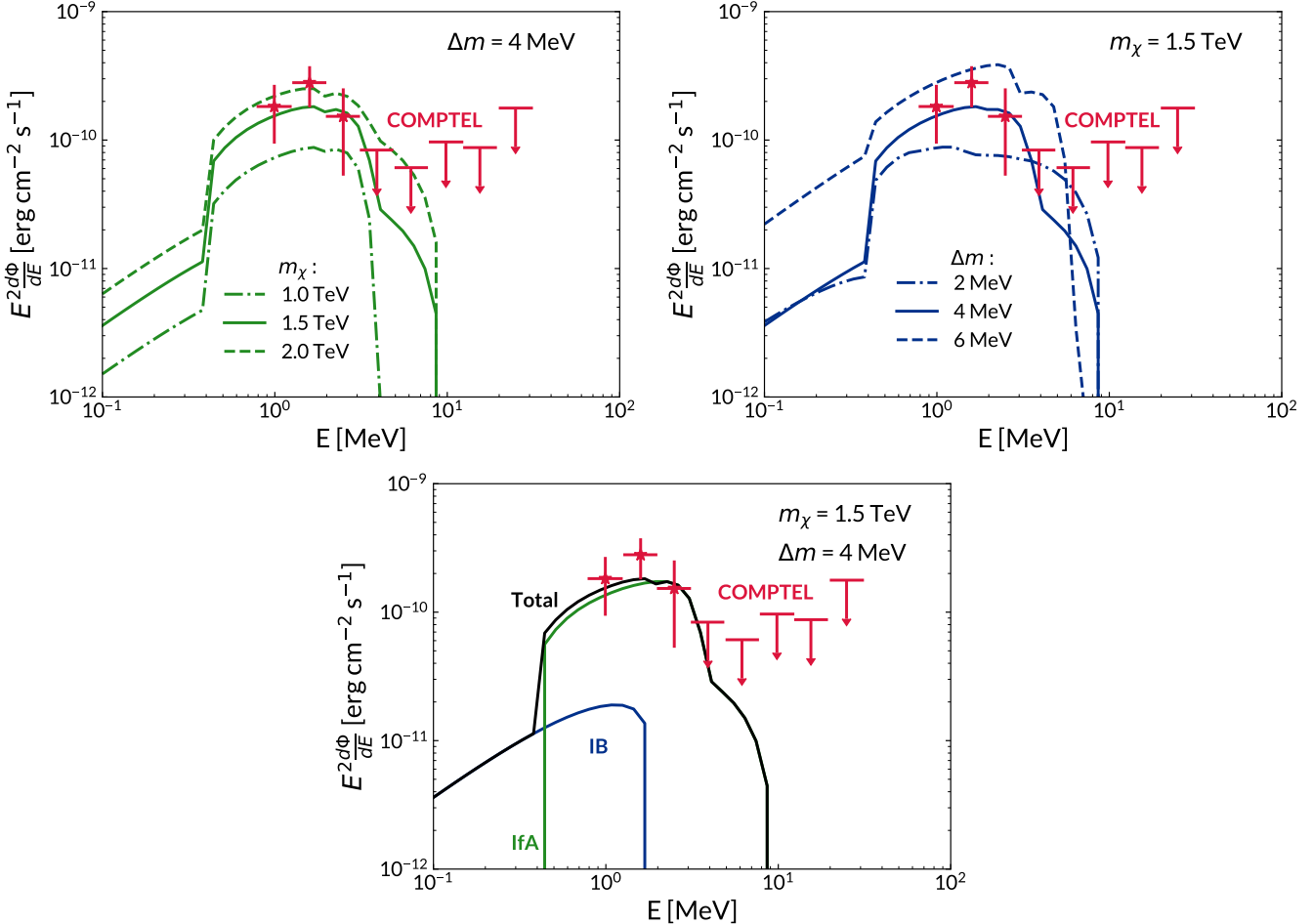


Figure 4. **Top-left:** COMPTEL IfA spectrum in the bulge region (red points) compared to XDM predictions for multiple m_χ with $\Delta m = 4$ MeV and σ_{mr} fixed by the 511 keV fit. **Top-right:** Same, for fixed $m_\chi = 1.5$ TeV and varying Δm . **Bottom:** Decomposition of the XDM signal for $m_\chi = 1.5$ TeV and $\Delta m = 4$ MeV into internal bremsstrahlung (IB, blue) and in-flight annihilation (IfA, green). The sum (black) is compared to COMPTEL data.

CR expectations and remaining relatively flat with radius, broadly consistent with the inferred profile (Oka *et al.* 2005; Oka and Geballe 2020; Ravikularaman *et al.* 2025) but still below the observed $\zeta_{\text{H}_2} \gtrsim 10^{-15} \text{ s}^{-1}$.

The normalization, however, does not fully saturate the observed CMZ ionization, which requires $\zeta_{\text{H}_2} \gtrsim 10^{-15} \text{ s}^{-1}$. Lower DM masses yield higher ionization rates, as they produce cuspier 511 keV and positron distributions. Similarly, cuspier DM profiles enhance the ionization near the GC, as shown in the right panel of Fig. 7 for the cNFW case, but at the price of a less uniform radial profile and tighter constraints from the 511 keV morphology.

Obolentseva *et al.* (2024) argued that ionization rates inferred for many molecular clouds across the Galaxy were biased high due to overestimates of their line-of-sight sizes and densities. This bias cannot by itself

account for the extreme ionization levels in the CMZ, whose geometry and gas properties are better constrained, but it may lower the inferred CMZ ionization somewhat. Allowing for such a downward revision, the XDM-induced contribution could lie closer to the true ionization level and plausibly account for a non-negligible fraction of the excess. A more dedicated treatment of CR and DM transport in the complex environment of the CMZ is needed to sharpen this conclusion, but our results already show that the same XDM parameter space that fits the SPI and COMPTEL data naturally produces a significant, radially flat ionization component in the CMZ.

4. DISCUSSION AND CONCLUSIONS

We have shown that a minimal XDM framework can account for three correlated Galactic anomalies with a sin-

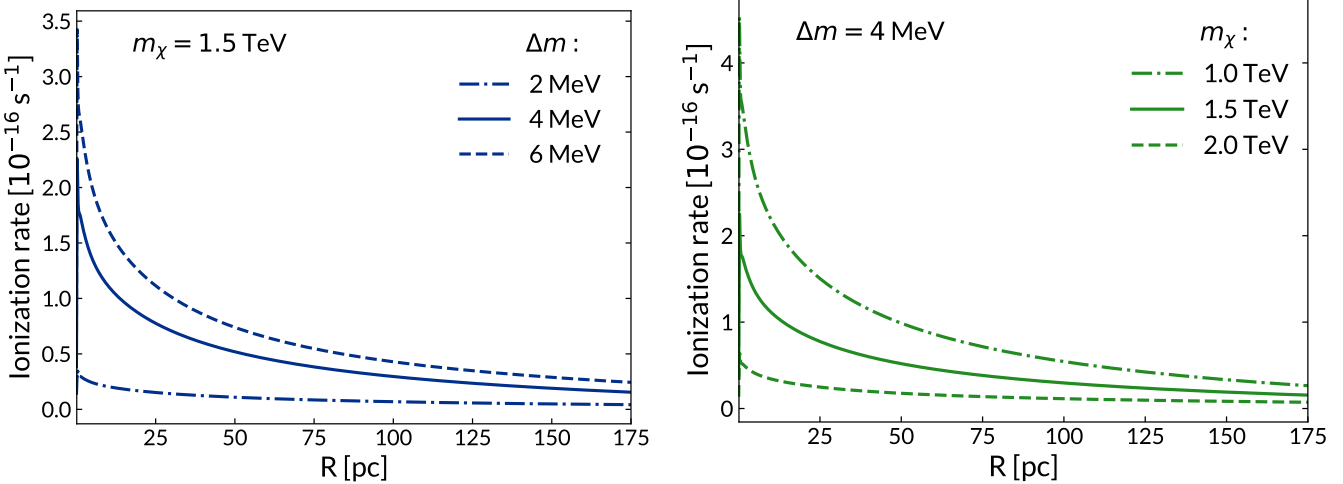


Figure 5. Radial profile of the H_2 ionization rate in the CMZ for XDM models as a function of cylindrical distance R from the GC. Left: fixed $m_\chi = 1.5$ TeV and varying Δm . Right: fixed $\Delta m = 4$ MeV and varying m_χ . All cases use NFW and the best-fit σ_{mr} from the 511 keV morphology.

gle mechanism. Inelastic upscattering $\chi\chi \rightarrow \chi\chi^*$ followed by $\chi^* \rightarrow \chi e^+ e^-$ injects few-MeV positrons that (i) reproduce the 511 keV morphology seen by INTEGRAL/SPI, (ii) generate the 2–3 MeV IfA excess reported in reanalyzed COMPTEL data, and (iii) provide a substantial, radially flat contribution to the anomalous ionization in the CMZ. In this sense, MeV-band observations, ionization measurements and the Galactic positron budget are all linked by the same dark-sector process.

Using DRAGON2, we performed the first full CR propagation calculation of positrons in the XDM context. For $\Delta m \simeq 3$ –6 MeV and TeV-scale m_χ , the resulting 511 keV longitude and latitude profiles are in strong agreement with SPI data, while the corresponding IfA spectrum matches the COMPTEL MeV bump within current statistical and systematic uncertainties. The same parameter space yields CMZ ionization rates $\zeta \sim 10^{-16}$ – 10^{-15} s^{-1} , larger than expected from standard CRs and with an approximately flat radial profile, although still below the nominal level inferred from molecular tracers. These late-time excitation rates can arise naturally from Sommerfeld enhancement in a light-mediator model and remain compatible with unitarity, thermal freeze-out and BBN constraints along the lines discussed in Finkbeiner and Weiner (2007).

A light boson of mass ~ 10 – 20 MeV coupling to e^\pm can play the role of the mediator in such XDM scenarios. Intriguingly, this mass range overlaps with the mild ($\sim 2\sigma$) excess near 16.9 MeV reported by the PADME experiment Bossi *et al.* (2025), suggesting that forthcoming fixed-target searches may begin to probe exactly the mediator parameter space relevant for such Galactic MeV signatures. In parallel, future “MeV gap” missions such as *COSI* Karwin *et al.* (2023); Siegert *et al.* (2020)

will provide sharper line and continuum measurements and improved morphology, offering a direct test of the correlated line and continuum predictions of XDM.

Beyond the Milky Way, massive galaxy clusters provide another promising arena. Their high velocity dispersions make inelastic upscattering efficient throughout the halo, potentially leading to non-thermal X-ray or γ -ray emission and small contributions to intracluster-medium heating. Current limits on diffuse cluster emission already require any such heating to be subdominant to active galactic nucleus feedback, but the possibility that DM–DM scattering produces modest intracluster heating or mild SZ distortions remains open and may be probed by upcoming high-sensitivity X-ray and SZ surveys Ade *et al.* (2019); Abazajian *et al.* (2016).

On cosmological scales, redshifted emission from XDM-induced e^\pm injection and associated CMB energy-injection constraints could test scenarios with substantial early-universe heating. Velocity-dependent self-interactions of the type considered here also remain relevant for small-scale structure, and related dissipative dark-sector dynamics have been proposed as a channel for rapid black-hole seed formation at high redshift. These ideas can be confronted with next-generation observations of high- z quasars and gravitational waves.

In summary, while extragalactic and cosmological signatures of XDM are still uncertain, the Galactic MeV window already unifies line emission, continuum excesses and molecular ionization in a coherent picture. If this interpretation is correct, the same few-MeV positrons that illuminate the GC in 511 keV photons are also leaving their imprint in the MeV continuum and in the chemistry of the CMZ, making MeV astrophysics a uniquely powerful probe of inelastic dark sectors.

5. ACKNOWLEDGEMENTS

SB is supported by the STFC under grant ST/X000753/1. DC acknowledges support from a Science and Technology Facilities Council (STFC) Doctoral Training Grant. PDL is supported by the Juan de la Cierva JDC2022-048916-I grant, funded by MCIU/AEI/10.13039/501100011033 European Union "NextGenerationEU"/PRTR. The work of PDL is also supported by the grants PID2021-125331NB-I00 and CEX2020-001007-S, both funded by MCIN/AEI/10.13039/501100011033 and by "ERDF A way of making Europe". PDL also acknowledges the MultiDark Network, ref. RED2022-134411-T. This project used computing resources from the National Academic Infrastructure for Supercomputing in Sweden (NAISS) under project NAISS 2024/5-666. This project used computing resources from King's College London CREATE system [King's College London](#). For the purpose of open access, the authors have applied a Creative Commons Attribution (CC BY) license to any Author Accepted Manuscript version arising from this submission.

APPENDIX

A. EXPECTED SIGNALS FROM A CONTRACTED NFW PROFILE

In this appendix we quantify the impact of adopting a cNFW profile, with inner slope $\gamma = 1.2$, instead of the standard NFW halo. For each profile we refit the 511 keV morphology to obtain the corresponding best-fit cross section σ_{mr} , which is quoted in the legend of Fig. 6 and used consistently in Figs. 7 and 8.

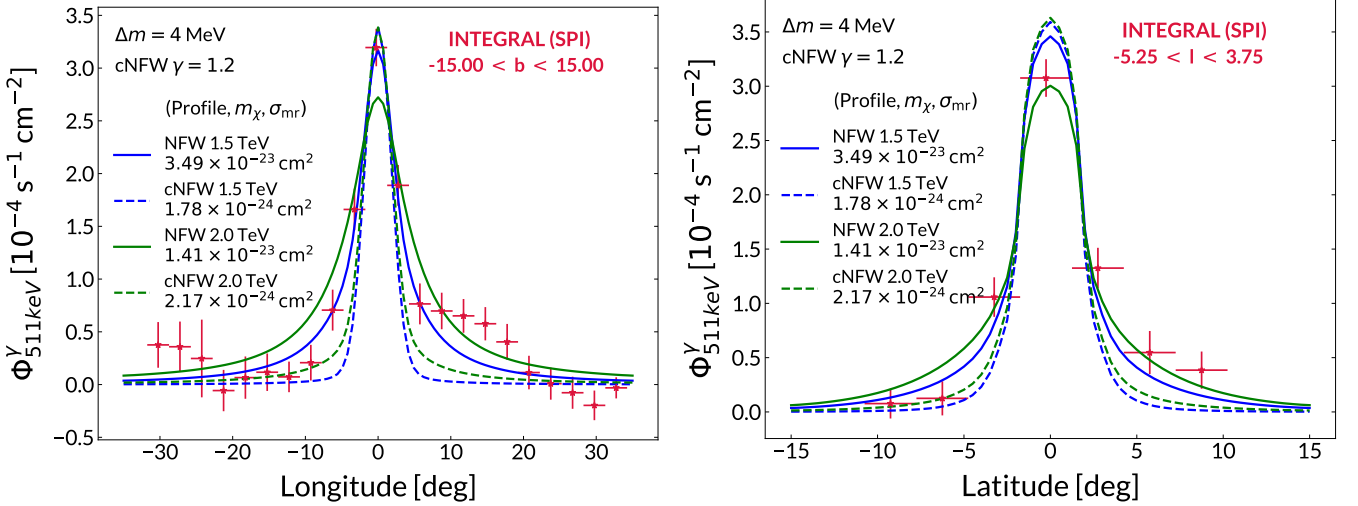


Figure 6. 511 keV longitude (left) and latitude (right) profiles for XDM models with $m_\chi = 1.5$ TeV (blue) and $m_\chi = 2$ TeV (green), and fixed mass splitting $\Delta m = 4$ MeV, compared to INTEGRAL/SPI data (red points). Solid lines correspond to an NFW profile, dashed lines to a cNFW profile. The best-fit values of σ_{mr} for each case are indicated in the legend.

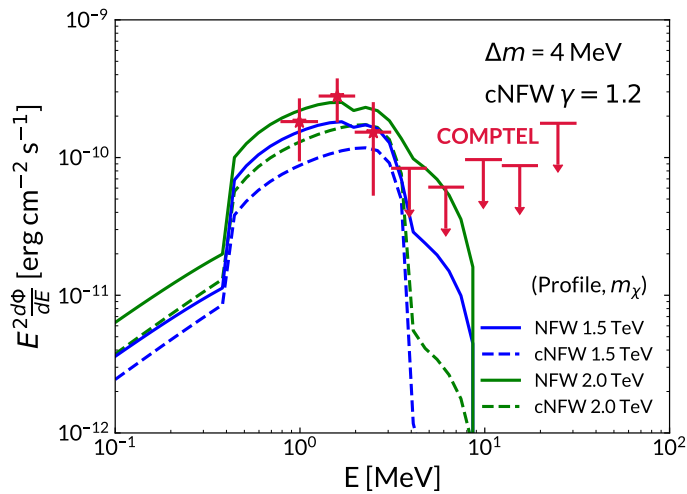


Figure 7. IfA flux measurements from COMPTEL (red points) compared to the XDM predictions for the same NFW and cNFW scenarios as in Fig. 6. The normalization in each case is set by the corresponding best-fit cross section σ_{mr} obtained from the 511 keV morphology.

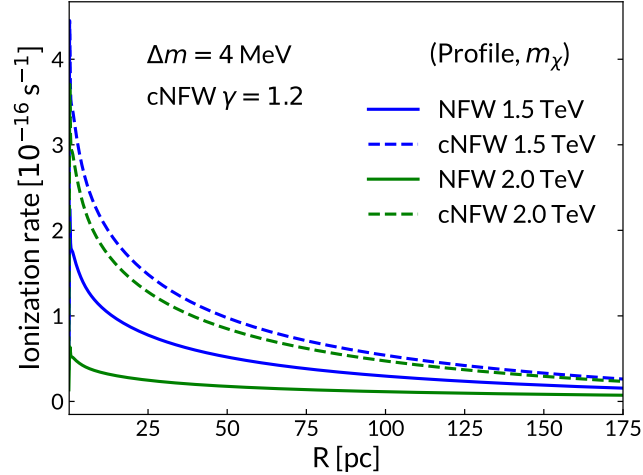


Figure 8. Radial profile of the H_2 ionization rate in the CMZ for the NFW and cNFW scenarios of Fig. 6. The normalization is again fixed by the best-fit σ_{mr} from the 511 keV fit.

REFERENCES

N. Prantzos *et al.*, *Rev. Mod. Phys.* **83**, 1001 (2011), arXiv:1009.4620 [astro-ph.HE]

C. A. Kierans *et al.*, “Positron annihilation in the galaxy,” (2019), arXiv:1903.05569 [astro-ph.HE]

T. Siegert, R. M. Crocker, R. Diehl, M. G. H. Krause, F. H. Panther, M. M. M. Pleintinger, and C. Weinberger, *Astron. Astrophys.* **627**, A126 (2019), arXiv:1906.00498 [astro-ph.HE]

T. Siegert, *Astrophysics and Space Science* **368** (2023), 10.1007/s10509-023-04184-4

R. Diehl *et al.*, *Astron. Astrophys.* **449**, 1025 (2006), arXiv:astro-ph/0512334

T. Siegert, R. M. Crocker, O. Macias, F. H. Panther, F. Calore, D. Song, and S. Horiuchi, *Mon. Not. Roy. Astron. Soc.* **509**, L11 (2021), arXiv:2109.03691 [astro-ph.HE]

M. M. Muru, J. Silk, N. I. Libeskind, S. Gottloeber, and Y. Hoffman, “Fermi-lat galactic center excess morphology of dark matter in simulations of the milky way galaxy,” (2025), arXiv:2508.06314 [astro-ph.HE]

C. Boehm *et al.*, *Phys. Rev. Lett.* **92**, 101301 (2004), arXiv:astro-ph/0309686

A. C. Vincent, P. Martin, and J. M. Cline, *JCAP* **04**, 022 (2012), arXiv:1201.0997 [hep-ph]

P. De la Torre Luque, S. Balaji, and J. Silk, *Phys. Rev. Lett.* **134**, 101001 (2025), arXiv:2409.07515 [hep-ph]

P. De la Torre Luque, S. Balaji, and J. Silk, *Astrophys. J. Lett.* **973**, L6 (2024), [Erratum: *Astrophys.J.Lett.* 991, L29 (2025)], arXiv:2312.04907 [hep-ph]

D. De la Torre Luque; Pedro, S. Balaji, M. Fairbairn, F. Sala, and J. Silk, *JCAP* **09**, 034 (2025), arXiv:2410.16379 [astro-ph.HE]

T. T. Q. Nguyen, P. De la Torre Luque, I. John, S. Balaji, P. Carenza, and T. Linden, (2025), arXiv:2507.13432 [hep-ph]

J. F. Beacom and H. Yuksel, *Phys. Rev. Lett.* **97**, 071102 (2006), arXiv:astro-ph/0512411

P. Sizun, M. Casse, S. Schanne, and B. Cordier, *ESA Spec. Publ.* **622**, 61 (2007), arXiv:astro-ph/0702061

R. J. Wilkinson, A. C. Vincent, C. Boehm, and C. McCabe, *Phys. Rev. D* **94**, 103525 (2016), arXiv:1602.01114 [astro-ph.CO]

M. Aghaie, P. De la Torre Luque, A. Dondarini, D. Gaggero, G. Marino, and P. Panci, arXiv e-prints (2025), arXiv:2501.10504 [hep-ph]

D. P. Finkbeiner and N. Weiner, *Phys. Rev. D* **76**, 083519 (2007), arXiv:astro-ph/0702587

C. V. Cappiello, M. Jafs, and A. C. Vincent, *JCAP* **11**, 003 (2023), arXiv:2307.15114 [hep-ph]

J. Knöldlseder, K. Sabri, P. Jean, P. von Ballmoos, G. Skinner, and W. Collmar, *Astron. Astrophys.* **700**, A257 (2025), arXiv:2506.17427 [astro-ph.HE]

T. Oka, T. R. Geballe, M. Goto, T. Usuda, and B. J. McCall, *The Astrophysical Journal* **632**, 882–893 (2005)

T. Oka and T. R. Geballe, *The Astrophysical Journal* **902**, 9 (2020)

S. Ravikularaman, S. Recchia, V. H. M. Phan, and S. Gabici, *Astronomy & Astrophysics* **694**, A114 (2025)

X. Huang, Q. Yuan, and Y.-Z. Fan, *Nature Communications* **12** (2021), 10.1038/s41467-021-26436-z

V. A. Dogiel, D. O. Chernyshov, V. Tatischeff, K.-S. Cheng, and R. Terrier, *The Astrophysical Journal* **771**, L43 (2013)

G. Weidenspointner *et al.*, *ESA Spec. Publ.* **622**, 25 (2007), [arXiv:astro-ph/0702621](https://arxiv.org/abs/0702621)

M. Pospelov and A. Ritz, *Phys. Lett. B* **651**, 208 (2007), [arXiv:hep-ph/0703128](https://arxiv.org/abs/hep-ph/0703128)

N. Arkani-Hamed, D. P. Finkbeiner, T. R. Slatyer, and N. Weiner, *Phys. Rev. D* **79**, 015014 (2009), [arXiv:0810.0713 \[hep-ph\]](https://arxiv.org/abs/0810.0713)

Jean, P. *et al.*, *A&A* **508**, 1099 (2009)

H. Nakanishi and Y. Sofue, *Publications of the Astronomical Society of Japan* **55**, 191–202 (2003)

K. Ferriere, *The Astrophysical Journal* **497**, 759 (1998)

F. W. Stecker, *apss* **3**, 579 (1969)

P. Sizun, M. Casse, and S. Schanne, *Phys. Rev. D* **74**, 063514 (2006), [arXiv:astro-ph/0607374](https://arxiv.org/abs/astro-ph/0607374)

A. W. Strong, K. Bennett, H. Bloemen, R. Diehl, W. Hermsen, D. Morris, V. Schoenfelder, J. G. Stacy, C. de Vries, M. Varendorff, C. Winkler, and G. Youssefi, *A&A* **292**, 82 (1994)

L. Bouchet, A. W. Strong, T. A. Porter, I. V. Moskalenko, E. Jourdain, and J.-P. Roques, *The Astrophysical Journal* **739**, 29 (2011)

J. F. Beacom, N. F. Bell, and G. Bertone, *Phys. Rev. Lett.* **94**, 171301 (2005), [arXiv:astro-ph/0409403](https://arxiv.org/abs/astro-ph/0409403)

L. Bouchet, J.-P. Roques, and E. Jourdain, *Astrophys. J.* **720**, 1772 (2010), [arXiv:1007.4753 \[astro-ph.HE\]](https://arxiv.org/abs/1007.4753)

R. Bartels, D. Gaggero, and C. Weniger, *JCAP* **05**, 001 (2017), [arXiv:1703.02546 \[astro-ph.HE\]](https://arxiv.org/abs/1703.02546)

M. Padovani, D. Galli, and A. E. Glassgold, *Astronomy & Astrophysics* **501**, 619–631 (2009)

J. Krause, G. Morlino, and S. Gabici, “Crime - cosmic ray interactions in molecular environments,” (2015), [arXiv:1507.05127 \[astro-ph.HE\]](https://arxiv.org/abs/1507.05127)

M. Obolentseva, A. V. Ivlev, K. Silsbee, D. A. Neufeld, P. Caselli, G. Edenhofer, N. Indriolo, T. G. Bisbas, and D. Lomeli, *The Astrophysical Journal* **973**, 142 (2024)

F. Bossi *et al.* (PADME), *JHEP* **11**, 007 (2025), [arXiv:2505.24797 \[hep-ex\]](https://arxiv.org/abs/2505.24797)

C. M. Karwin, T. Siegert, J. Beechert, J. A. Tomsick, T. A. Porter, M. Negro, C. Kierans, M. Ajello, I. Martinez-Castellanos, A. Shih, A. Zoglauer, and S. E. Boggs, *The Astrophysical Journal* **959**, 90 (2023)

T. Siegert, S. E. Boggs, J. A. Tomsick, A. C. Zoglauer, C. A. Kierans, C. C. Sleator, J. Beechert, T. J. Brandt, P. Jean, H. Lazar, A. W. Lowell, J. M. Roberts, and P. v. Ballmoos, *The Astrophysical Journal* **897**, 45 (2020)

P. Ade *et al.* (Simons Observatory), *JCAP* **02**, 056 (2019), [arXiv:1808.07445 \[astro-ph.CO\]](https://arxiv.org/abs/1808.07445)

K. N. Abazajian *et al.* (CMB-S4), *CMB-S4 Science Book, First Edition* (2016) [arXiv:1610.02743 \[astro-ph.CO\]](https://arxiv.org/abs/1610.02743)

King’s College London, “King’s Computational Research, Engineering and Technology Environment (CREATE),” Retrieved December 10, 2025, from <https://doi.org/10.18742/rnfv-m076>